Engineering Structures 325 (2025) 119445

Contents lists available at ScienceDirect

Engineering Structures

journal homepage: www.elsevier.com/locate/engstruct

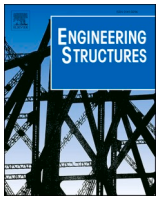

Structural health monitoring (SHM) on a long semi-integral high-speed railway bridge (HSRB) under different traffic loads

Sisi Zhang [a,*], Max Käding [b], Marc Wenner [b], Martin Claßen [a], Steffen Marx [c]

[a] Institute of Structural Concrete, RWTH Aachen, Germany
[b] MKP GmbH, Germany
[c] Institute of Structural Concrete, TU Dresden, Germany

ARTICLE INFO

Keywords:
Structural health monitoring (SHM)
High-speed railway bridge (HSRB)
Semi-integral bridge
Braking loads
High-speed traffic
Monolithic piers
Static and dynamic behavior

ABSTRACT

In this paper, the structural behaviour of a long semi-integral HSRB, i.e., Unstrut Viaduct, under different traffic loads was studied by both SHM and static calculation using numerical simulation. The demanding requirements of semi-integral HSRB for both flexibility and rigidity were assessed by measuring the deformation of the superstructure and piers under quasi-static loads, as well as the structural responses under braking and high-speed loads, respectively. The results showed that the separating pier of the semi-integral bridge enables larger deformation freedom, which is beneficial to reducing the restrained stresses due to temperature, creep and shrinkage. The separated superstructure here would induce larger pier curvature and a greater warping effect under single-track loading. The coupling of continuous welded rail (CWR) at the bridge joint and the H-connection of the separating pier pair also caused the complex interaction of the two connected structural blocks. The rigidity of the semi-integral HSRB under braking and high-speed loads was also proven. The dynamic longitudinal stiffness under braking loads derived from measurements is unexpectedly 12 times that in the static calculation, showing the robustness and great load-bearing potential of the semi-integral bridge. The initial assumption in the static calculation, which treats the slab track as external loads without stiffness, is a conservative approach. However, incorporating both the mass and stiffness of the slab track into the model generally offers a more realistic prognosis.

1. Introduction

Compared to road bridges, the significantly higher traffic loads, increased braking and traction forces, and stringent deflection limits are crucial factors in the design of railway bridges. On the high-speed railway line between Erfurt and Leipzig, a new structural concept of integral and semi-integral viaducts has been designed and constructed for the first time in Germany [1–5]. Special SHM was conducted during the construction, the startup phase, and the first operation year to evaluate the actual structure behaviour of this new kind of HSRB [6–8]. This paper will study and display short-term monitoring results and their comparison with static calculations in the design phase.

1.1. State-of-art on the integral and semi-integral bridges

Traditional simply and continuously supported bridges, relying on bearings and expansion joints, are increasingly being replaced due to recurring maintenance challenges and operational inefficiencies. Meanwhile, integral and semi-integral bridges have emerged as robust alternatives, offering improved durability, maintenance, and load-bearing capacity [10–14].

Integral bridges, characterized by their continuous and joint-free design, eliminate the need for movable components and create a seamless connection between all parts of the bridge, cf. Fig. 1 (1), which is gaining traction for their ability to enhance load distribution and reduce maintenance costs [12,13]. This construction approach also offers significant benefits under dynamic loading conditions, such as those in seismic areas [15,16] or experienced in high-speed rail operations [17], where the demand for structural redundancy and system reliability is paramount. The fixed restraints on both sides can reduce the buckling length of the piers, allowing for a greater range of span choices [13]. Furthermore, eliminating joints and transition structures results in smoother ride comfort and lower noise emissions [10], which is also a critical factor in HSRB applications. However, The rigid monolithic

* Corresponding author.
E-mail address: sisi.zhang@rwth-aachen.de (S. Zhang).

https://doi.org/10.1016/j.engstruct.2024.119445
Received 15 January 2024; Received in revised form 20 November 2024; Accepted 2 December 2024
Available online 9 December 2024

design leads to substantial challenges in accommodating longitudinal movements caused by temperature, creep, and shrinkage, often necessitating extensive geotechnical analysis to mitigate the effects of settlement-induced stresses [18–20]. Planning or execution errors are challenging to rectify after construction, requiring precise design with advanced modelling to account for realistic parameters, restrained stresses, and potential cracks in the ultimate limit state [14].

Semi-integral bridges offer a balanced solution, providing a compromise between the benefits of integral designs and the flexibility of traditional designs. By incorporating at least one expansion joint, these bridges can better accommodate longitudinal movements, thereby reducing constraint stresses in the superstructure [21–23]. This adaptability makes them particularly suitable for longer spans and challenging terrain, such as wide valleys, where the combined requirements of structural deformability and rigidity must be carefully balanced [4]. However, the longitudinal movement of the deck induces bending moments in the piers due to pier head displacements, requiring careful design of slender piers and optimized structural systems to manage these stresses [24]. Additionally, the demands for horizontal stiffness for railway bridges due to braking and traction forces necessitate non-displaceable or quasi-nondisplaceable supports [5]. Recent studies have focused on addressing these challenges through innovative solutions. For example, research on semi-integral bridges has explored various strategies for the design of fixed points, including the use of damper systems to absorb horizontal forces during fast displacements while allowing slow displacements to occur freely, cf Fig. 1 (2) [9].

In sum, semi-integral bridges offer significant long-term benefits in durability and load-bearing capacity but require careful design to balance deformability and rigidity, especially for HSRB, where the traffic loads are much larger. Addressing these challenges enables the creation of future robust, efficient, and sustainable structures.

1.2. The Unstrut Viaduct

The Unstrut Viaduct is one of the innovative semi-integral bridges in the new high-speed railway line between Erfurt and Leipzig in Germany [5]. The viaduct consists of four integral structure sections with span widths of 4×58 m – 116 m – 4×58 m for each section, constructed against each other with two approach bridges of 3×58 m at two sides. For each integral section, the continuous box girder is monolithically connected with column piers at two sides while jointed with an arch at the middle of the system, where no bearing is needed. C40/50 concrete and 500 S reinforcement were used for the superstructure, piers and arches. The arch has a span width of 108 m and serves to carry the brake and traction forces. The two approach bridges are mounted horizontally unmovablely on the abutments at two sides. The ÖBB-PORR slab track system is used on the bridge for the rail, while the ballast lays only in between the two slab tracks rather than being an essential functional component, cf. Fig. 2. The piers are rectangular in cross-section and taper downward with an inclination of 1:40 in the transverse direction, while the width remains constant in the length direction. The main dimensions of the box girder, piers and foundation can be found in Fig. 3.

2. Monitoring concept

2.1. Concept and layout

Since the integral and semi-integral bridges were first applied in railway lines in Germany, experiences regarding the actual behaviour of the structure were missing when guidelines were drafted. In order to prove the assumptions in the calculation model as well as collect practical structure information, monitoring, including long-term and short-term measurements, was implemented [25–28].

The general measurement concept for Unstrut Viaduct consists of (1) long-term behaviour, where superstructure deformations due to temperature, creep and shrinkage were monitored; (2) short-term behaviour under traffic loads, where longitudinal and rotation deformations of the bridge joints, bending rigidity of the monolithic piers under quasi-static traffic trains, the longitudinal stiffness under braking loads as well as dynamic characteristics of the bridge under high-speed traffic loads were measured. In this paper, the focus lays on the short-term behaviour under traffic loads. The chosen monitoring layout to answer the questions above consists of the following measurements: (1) *JLD*, longitudinal displacements at bridge joints; (2) *PS*, strain at pier head; (3) *ER*, end rotation of the superstructure; (4) *A*, acceleration for high-speed tests, see Fig. 3.

The relative longitudinal displacements at bridge joints were recorded by three linear variable displacement transducers (LVDT) at each joint. Meanwhile, the strains at the pier head were measured at four corners of the investigated piers by reinforcement bars with pre-applied strain gauges. Moreover, tilt sensors were installed at bridge joints of axis 33 and axis 44 for the detection of the end rotation of the superstructure. To obtain the dynamic behaviour of the structure under high-speed traffic loads, temporary IEPE Accelerometers with a measurement range of +/- 6 g and a resolution of ca. 1.2×10^{-6} g were installed on the superstructure at four selected locations between axis 40 and axis 43. Two vertical accelerators and one horizontal accelerator were set at each location so that the first three vertical and horizontal natural

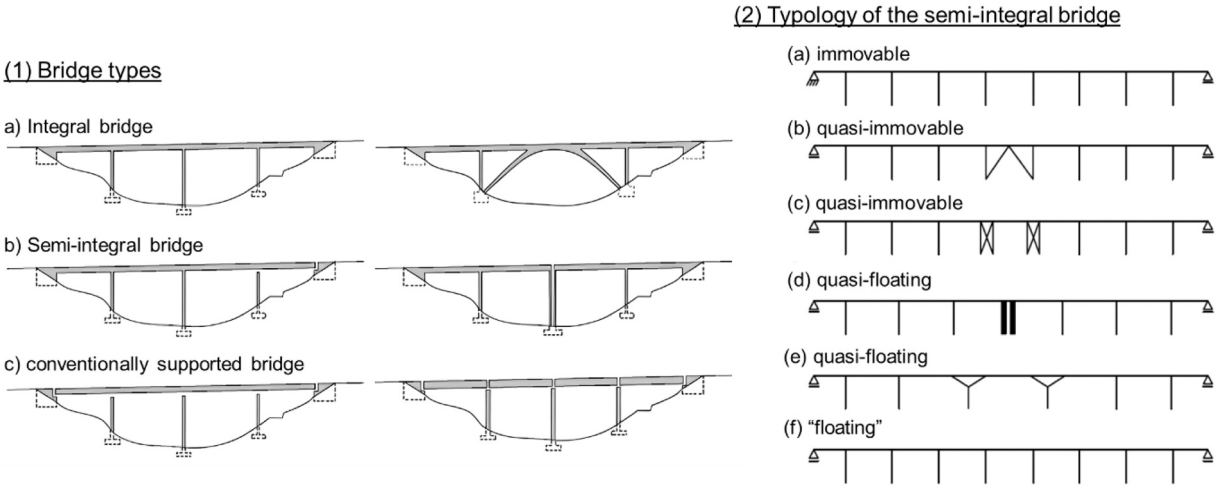

Fig. 1. Schematic illustration of (1) different bridge types of integral, semi-integral, and conventionally supported bridges, and (2) various topologies of semi-integral bridge [9].

Fig. 2. Photograph of the Unstrut Viaduct.

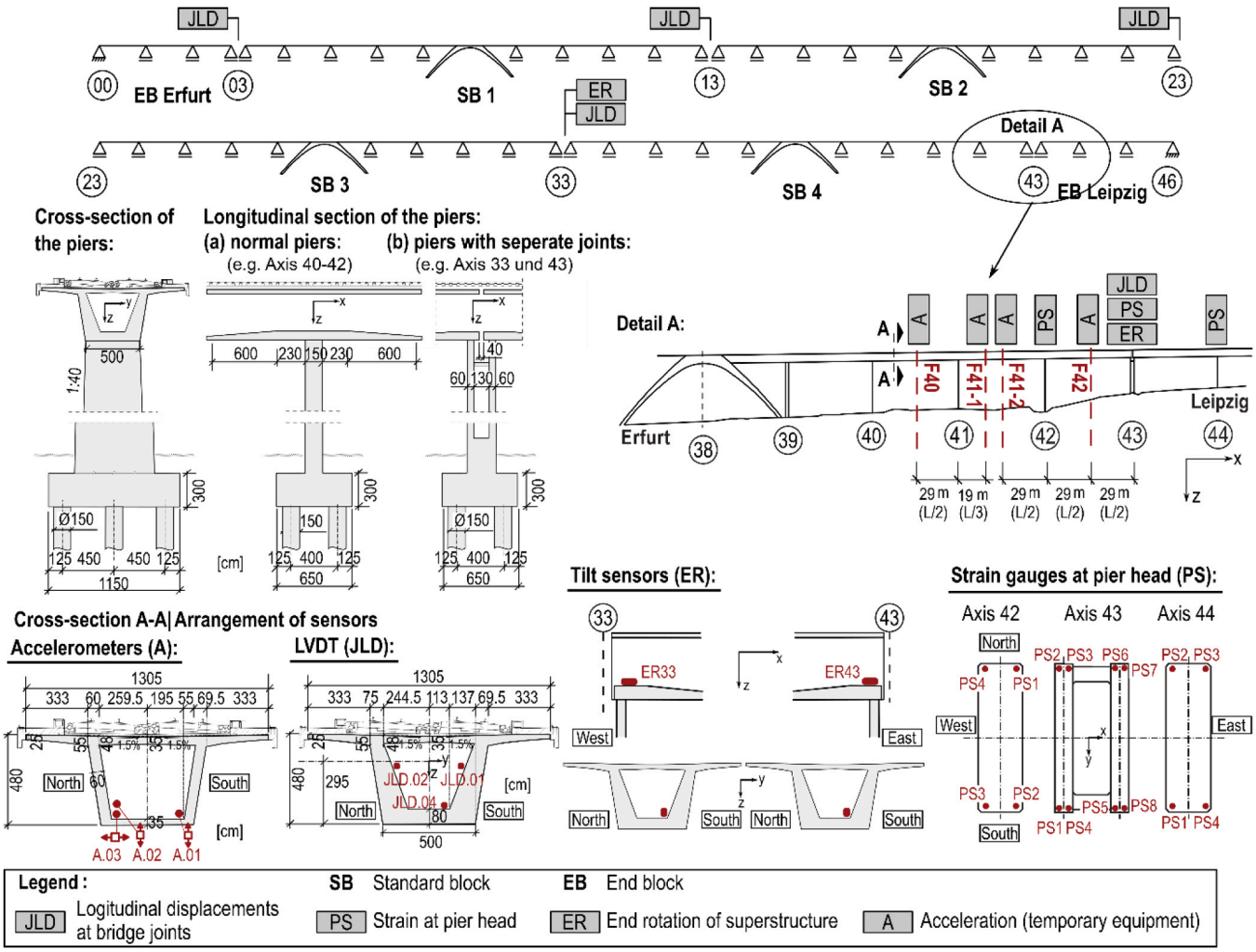

Fig. 3. Overview of the Unstrut Viaduct layout with various measurements.

frequencies, as well as their corresponding eigenmode and damping ratio, could be evaluated. The sampling frequency of the sensor used in this paper is 500 Hz.

2.2. *Traffic constellation in the test phases*

Short-term experiments with two freight trains filled with ballast (Fig. 4) were performed to describe the behaviour under quasi-static vertical and braking loads. The accelerometers were employed at four measurement points on the train to measure the acceleration of the train in braking tests. In order to distinguish the movements of trains from the structural reactions, additional GPS equipment was used to record the movements of trains. To synchronise the measuring systems on the structure and on the train, a light-trigger and a reflector were installed on the track; meanwhile, another light-trigger was built on the train. The distance between the light-trigger on the train and the first axis on the Erfurt side corresponds to the distance between the reflector plate and the light-trigger on the track (Fig. 4). When the wheel passes the light-trigger on the track, or the light-trigger on the train passes the reflector plate on the track, a deflection is generated in the signal curve. Based on these deflections, the channels of the measuring systems could be superimposed and compared with each other.

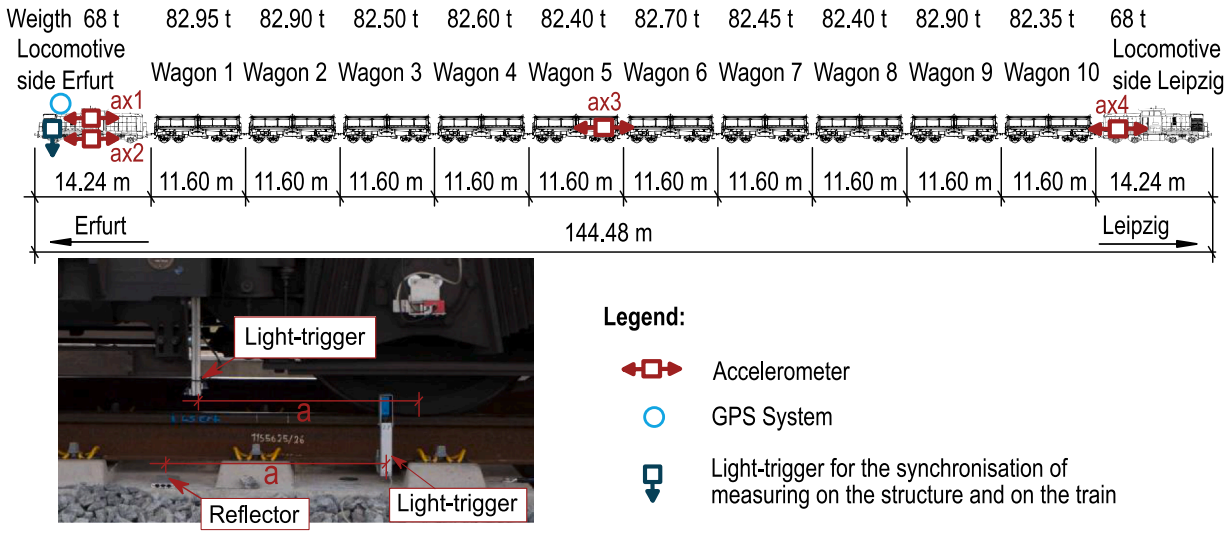

Fig. 4. Instrumentation of the freight trains.

Besides, high-speed passages with ICE-S provided by DB AG (Fig. 5) were implemented, which consist of two locomotives and two carriages. Unlike freight trains, where wheel loads are determined by the self-weight of each wagon including ballast, this experimental train ICE-S has its axle loads pre-measured at the factory, with the values already provided. In this paper, three kinds of traffic loads were conducted by the two kinds of trains to investigate different reactions of the bridge.

2.2.1. Quasi-static train passages

In order to induce possible quasi-static loads at the bridge, freight trains ran on the bridge with a low speed of about 10 km/h and loaded not only on single track but also on double track:

- QS 1: The train travelled at a low speed of 10 km/h on the south track of the Viaduct, making two round trips in each direction.
- QS 2: The train travelled at a low speed of 10 km/h on the north track of the Viaduct, making two round trips in each direction.
- QS 3: The train travelled at a low speed of 10 km/h parallel on both the south and north tracks of the Viaduct, making two round trips in each direction.

A total of 12 quasi-static train passages in both travelling directions over the structure were recorded. The measurement results of rotations at the bridge beam ends, as well as the rotations at the pier head, will be compared with the calculated results.

2.2.2. Braking train passages

Following the quasi-static train passages, the braking forces from one freight train were loaded at different braking positions on the south track with a speed of 20 km/h in the structure section between axes 33 and 43 (Fig. 6).

The braking positions (BP) could be described as the following:

- BP1: last wheel axle of locomotive at Leipzig side at 10 m ahead of axis 43, travelling direction from Leipzig to Erfurt on the south track.
- BP2: first wheel axle of locomotive at Erfurt side at axis 38, travelling direction from Leipzig to Erfurt on the south track.
- BP3: first wheel axle of locomotive at Erfurt side at 15 m after axis 33, travelling direction from Leipzig to Erfurt on the south track.
- BP4: first wheel axle of locomotive at Leipzig side at 10 m ahead of axis 43, travelling direction from Erfurt to Leipzig on the south track.

The trains were accelerated to a maximum speed of 20 km/h and braked quickly to the planned position at a sufficient distance. The braking distance was about 24 m. Four to five braking experiments were conducted for each braking position on the south track so that statistical results could be obtained. The correlation between braking forces and longitudinal displacements at joints from measurements will be described, while the stiffness will be evaluated from regression of the force-displacement curve.

2.2.3. High-speed train passages

The high-speed train increased its speed step by step to 330 km/h, whereas the return trips were made at a speed of approximately 160 km/h. At the beginning of each measurement day, a so-called blocking run with a speed of approximately 40 km/h was carried out to visually check the track for obstacles. In sum, 68 train passages with various travelling speeds were recorded and used for the evaluation, in which 35 travellings ran on the south track and 33 travellings ran on the north track. Except for the 3 travellings on the south track which were only recorded in the direction from Leipzig to Erfurt, the other 32 travellings on the south track were recorded as 16 round-trip travellings

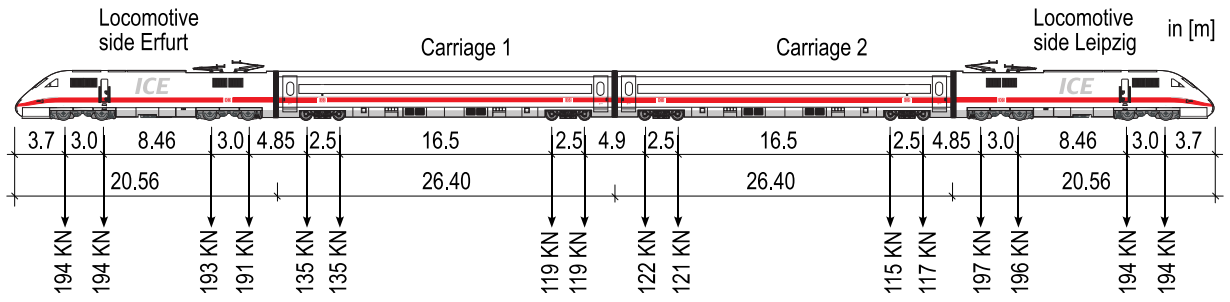

Fig. 5. Configuration of the high-speed train ICE-S.

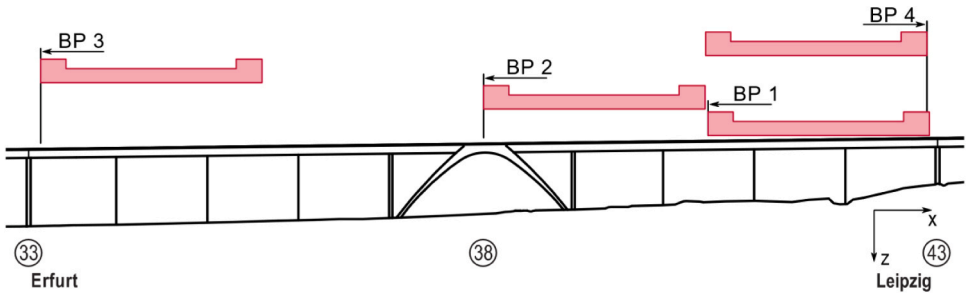

Fig. 6. Braking positions in the investigated structure section on the south track.

in both directions. Similarly, for the north track, except for the 3 travellings that only recorded trips from Erfurt to Leipzig, the other 30 travellings were 15 round trips in both directions.

3. Numeric model

To compare the measurement results, the bridge was partly modelled from axis 33 to axis 46 with the software SOFiSTiK, see Fig. 7. 3D Beam elements were used to model box girder superstructure, piers, and arch. The superstructure is fixed coupled with piers and the arch by means of a rigid connection. The geometry and material parameters of the structure are the same as the original assumptions in the design phase. A linear elastic material model for reinforcement concrete with an E-module of 31400 MN/m^2 and a density of 2400 kg/m^3 for C40/50 was used for the superstructure, piers and fundaments in the model based on DIN EN 1992–2:2010–12 [29]. The piers are connected to the superstructure using fixed coupling. Meanwhile, the longitudinal slope of the superstructure with the value of 12.5 ‰ is also considered in the model by adjusting the z-coordinates of the box girder beam elements. At axes 33 and 43, the separate joints (SJ) are modelled where the superstructure is discontinuous, but its piers on both sides are connected to the same foundation (at axis 33, only one pier on the simulated superstructure part was modelled at SJ), see Fig. 7. The geometries of the superstructures, piers and foundations in the model are consistent with the actual structure, see Fig. 3.

In the original design based on DIN EN 1991–2:2010–12 [30], DIN EN 1992–2:2010–12 [29] and DIN Fachbericht 101:2009–3 [31], the influence of slab track and bridge capes were considered as external loads similar to the ballast track. However, a bending stiffness increase is expected since the slab track system lays on the superstructure and is coupled with bridge caps, protective concrete cover, and waterproofing layers. As a result, the influence of the slab track system will be investigated with a parameter study and compared with the measurement results. A concrete plate of 13.05 m x 0.4 m was longitudinal continuously coupled with superstructure as a simplification in the first step, which leads to a 41.5% increase in the bending stiffness.

The semi-integral structure is anchored at each axis by its foundation at axes 33–45 and abutment at the bridge end at axis 46, while the foundation/ abutment stiffness is modelled with linear springs (C_x, C_y and C_z) and torsion springs ($C_{\varphi,x}$, $C_{\varphi,y}$ and $C_{\varphi,z}$) according to the information of static calculation. In axes 37 and 39, the pier and the arch are founded on the same foundation so that the deformations of the pier and arch are coupled in all directions at each foundation. The equivalent spring stiffnesses of pile foundation systems were determined by FE programs to analyse pile groups modelled as frameworks, considering the nearby subsoil and beneath the pile group cap using elastic foundation methods based on empirical values. This approach assumes variable foundation stiffness with depth and constant stiffness under the foundation. The subsoil's reaction varies with displacement caused by loads from piles or pile caps, which can be managed by iteratively adjusting the foundation stiffnesses [8]. Further details regarding this approach are available in the publication "EA piles" by the German Society for Geotechnics [32]. In this paper, the modelling focuses on the integral structure including superstructure and piers/ arches. The values

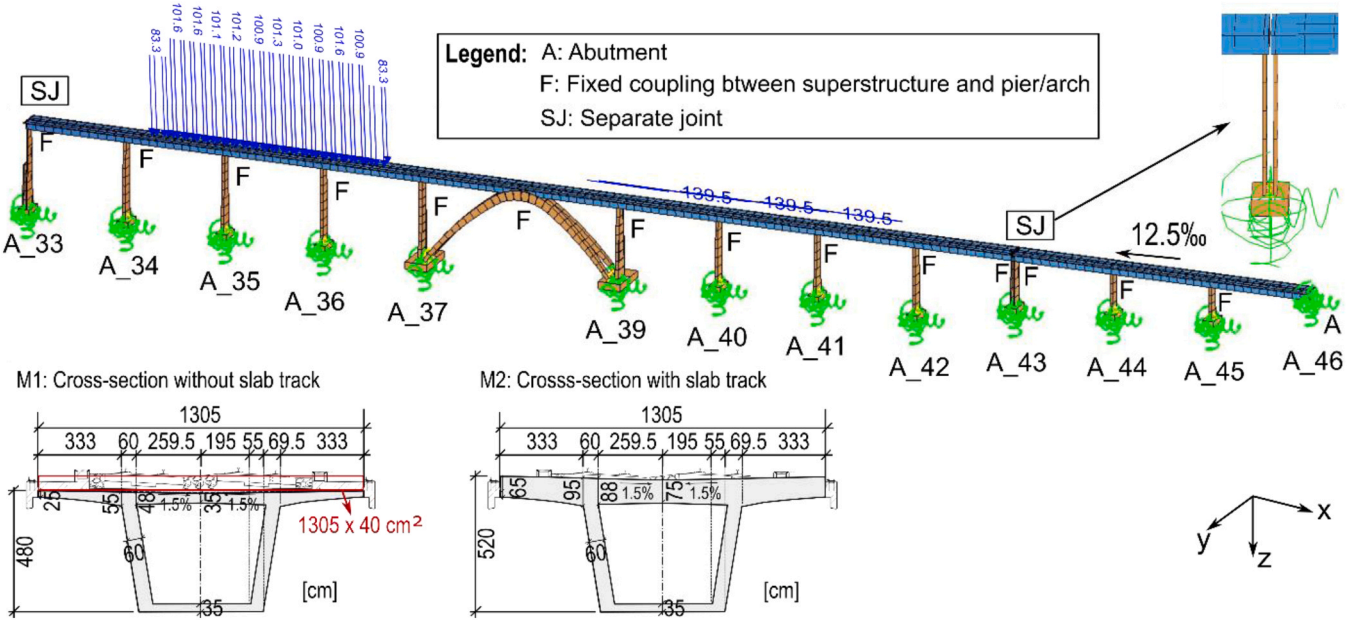

Fig. 7. Description of the FEM for Unstrut valley viaduct.

of stiffnesses for each foundation axis are listed in Table 1.

The vertical train loads are modelled by converting the actual wagon weight into wheel loads and calculated in 1 m intervals to determine the influence line. On the other hand, the braking force is simulated as a longitudinal uniformly distributed load along the train length according to the assumption in DIN EN 1991–2:2010–12 chapter 6.5.3 [30], which is calculated based on the measured acceleration and actual axle loads. For the integral structure, the foundation stiffness and the bending stiffness of the slender piers significantly influence stresses in the structure, especially at the pier head. To illustrate possible reasons for the discrepancies between measurement and calculation results, parametric evaluation of different stiffness configurations was implemented as follows:

- M1: without consideration of slab track and bridge caps (abbreviated to slab track), which corresponds to the original static calculation, where the weight of slab track is considered as external loads, but the stiffness of slab track is not considered.
- M2: with consideration of both the weight and stiffness of the slab track, where the cross-section area of the box-girder top is increased by 13.05×0.4 m^2.
- M3: reduction of foundation stiffness in all directions in Table 1 by 20%, with slab track.
- M4: reduction of foundation stiffness in all directions in Table 1 by 20%, without slab track.
- M5: reduction of the E-modulus of the piers by 20% (here 31400 MN/m^{2}x0.8 =25120 MN/m^2), with slab track.

In the FEM, the soil stiffness corresponds to the mean values provided in the geotechnical report, while the scatter of geotechnical values is known to be very high. According to Ril 804.4501 [33], which regulates the design of integral and semi-integral railway bridges in Germany, the modulus of subgrade reaction must be variated from 0.5 times the mean value for the lateral stiffness of a pile foundation or 0.75 times the mean value for the vertical stiffness up to 5 times the mean value for both lateral and vertical stiffness to assess the consequences on the structural stresses and deformations in extreme cases. The 20% reduction in foundation stiffness in M4 is considered realistic. On the other hand, the stiffness characteristics of the piers correspond to the uncracked section, whereas possible cracks in practice could lead to reduced stiffness. The stiffness reduction accounts for the typical variability in the e-modulus of concrete, which can be estimated at ± 20%. Since measurement results show the structure exhibits greater flexibility, a 20% stiffness reduction has been incorporated into model M5.

4. Results of the measurement and comparison with the model

4.1. End rotation of the superstructure

The relative displacements at the bridge joints of axes 33 and 43 were recorded by three LVDTs at each cross-section (cf. Fig. 3). The measured relative displacements are a superposition of the relative longitudinal displacements and rotations around the y-axis and z-axis between the adjacent superstructure ends. With the help of the known positions of the sensors, the total deformation can be decomposed into its individual deformation components (i.e., longitudinal displacements, rotation around the y-axis and rotation around the z-axis). The calculation is referenced to the centre of gravity of the superstructure. On the other hand, the tilt sensor at the bridge joints of axes 33 and 43 measured the absolute rotations around the y-axis of the superstructure ends. The positive relative displacement and relative and absolute rotation are defined in the following Fig. 8.

4.1.1. The influence lines of superstructure end rotations

Fig. 9 displays the average results of the influence line of the absolute rotation at axis 33 for two round trips under corresponding quasi-static loads, where the position of the load is given as the abscissa of the first wheel axle of the locomotive at side Erfurt in the local coordinate system. The inclinations of the superstructure under double-track loadings show a superposition effect of the single-track loadings with extremes of the deformations of approximately twice as large. Since the tilt sensors were located on the south side of the girder, larger measured maximum values were detected for train passages running on the south track (QS 1).

At axis 33, the maximum value of the rotation occurs when the first wheel axle of the locomotive at the Leipzig side is above the structure axis 34, i.e., both end spans of the standard block (SB) 3 and 4 loaded. The minimum value is set when the first wheel axle of the locomotive at the Erfurt side is above structure axis 34, i.e., the penultimate span of SB 4 is loaded, and the end span of SB 4 is not loaded. A similar phenomenon regarding maximum and minimum end rotation at axis 43 could also be found for train loading on the other side of SB 4.

4.1.2. Comparison of measurement results with the calculated results

Fig. 10 compares the extreme values of the absolute end rotation from the calculations and measurements in axis 33, where the measured extreme values are the mean values of all the extreme values of corresponding quasi-static train passages. The figure shows that the measured extreme values are smaller than the calculated ones in the model without slab track (M1) but similar to the ones in the model with slab track (M2). For single-track loading, the measured values are smaller than the calculated ones in both models, whereas the measured values lie between the calculated values from the model with (M2) and without (M1) slab track for double-track loading. Thus, the increased superstructure stiffness considering slab track (M2) leads to greater deformation reduction compared to M1 under large (i.e., double-track) loading. The measured extreme absolute end rotations detected by tilt sensors on the south side of the girder under south-track loading (QS1) are larger than those under north-track loading (QS2), primarily due to the torsional effect. This phenomenon could nevertheless not be

Table 1
The equivalent spring stiffnesses of pile foundations.

Axis	C_x [MN/m]	$C_{\varphi,x}$ [MN/rad]	C_y [MN/m]	$C_{\varphi,y}$ [MN/rad]	C_z [MN/m]	$C_{\varphi,z}$ [MN/rad]
33	372	16393	444	9804	2899	42553
34	364	58824	435	20408	3802	9434
35	394	60606	469	21277	3984	9901
36	498	55556	585	20833	3704	12821
37	2551	699301	2882	259740	15504	202840
39	2591	704225	2732	259740	15504	204082
40	474	58824	552	21053	3759	11905
41	215	55556	246	18868	3610	5000
42	239	52632	273	18182	3448	5714
43	148	45455	166	16393	3125	3472
44	221	50000	255	17857	3333	5435
45	667	62500	781	22727	4082	16949
46	471	73368	383	2150	4649	20024

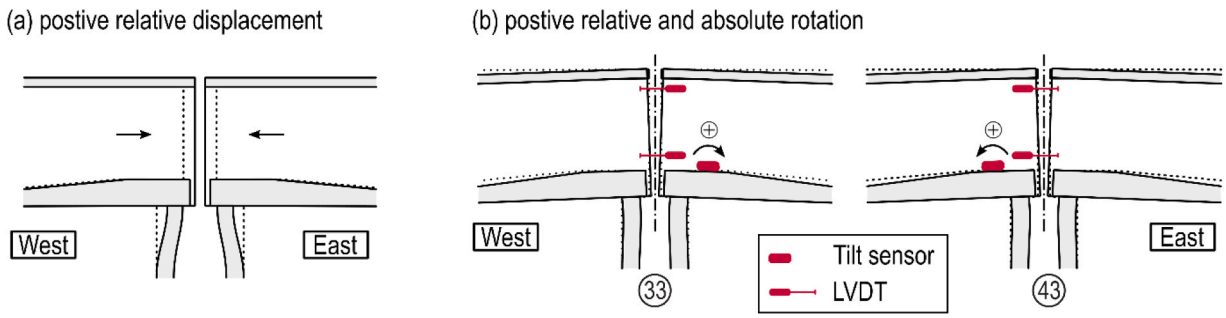

Fig. 8. Definition of positive relative displacement, relative and absolute rotation.

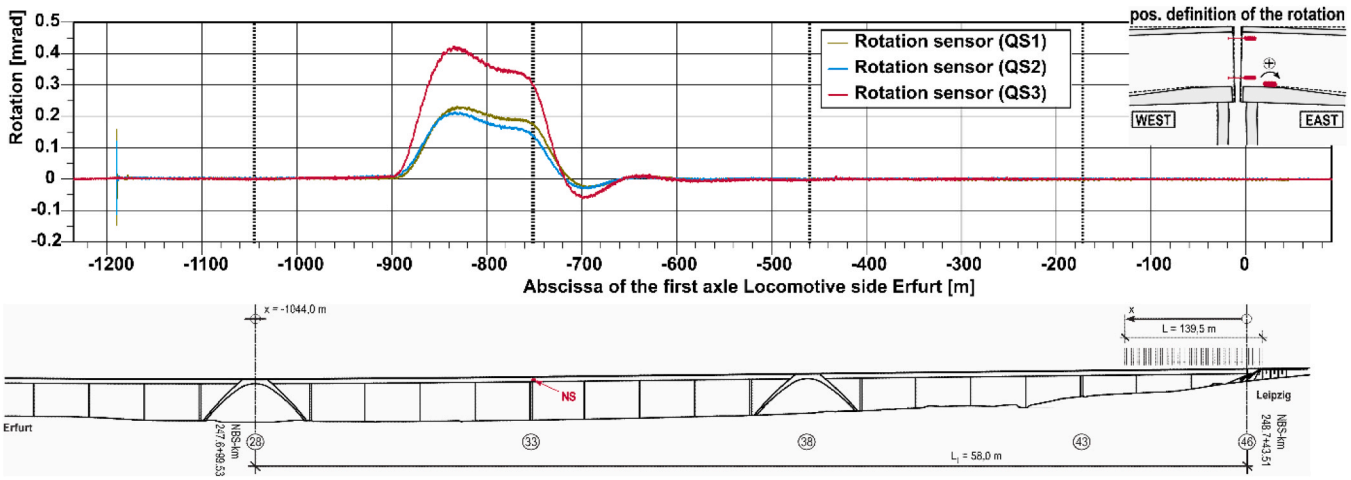

Fig. 9. Influence lines of the absolute rotations at axis 33 under quasi-static loads.

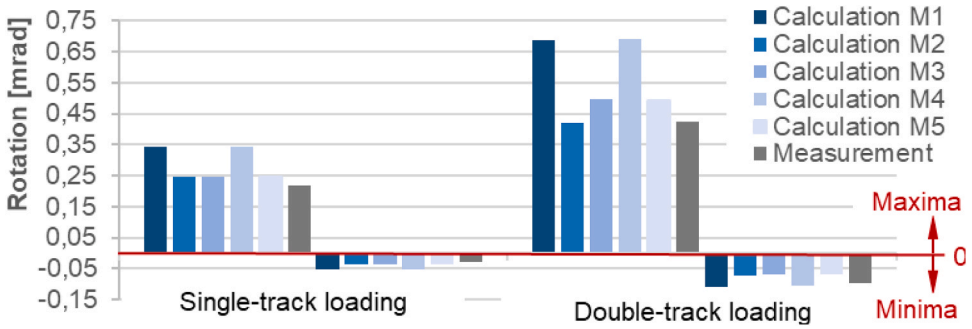

Fig. 10. Calculated and measured extreme absolute end rotation of the superstructure in axis 33.

observed from numerical models employing beam elements even though eccentric loadings were used for single-track scenarios. To simulate the torsional deformation, volume or shell elements, which account for cross-section deformation, are recommended. However, given that the observed differences are relatively minor and our main focus is on vertical and longitudinal deformations, utilizing beam elements for modelling the entire bridge offers superior efficiency.

The foundation and pier stiffness have limited influence on the end rotation of the superstructure, especially for single-track loading. The model with slab track on double-track loading is more sensitive to the variation of foundation and pier stiffness, whereas the model with slab track on single-track loading and the model without slab track on double-track loading are less influenced by the foundation and pier stiffness variations.

In sum, a good qualitative agreement between the measured and calculated results was seen. The best approximation between the curves from measurement and calculation was observed when the coupling of the slab track system into the superstructure was considered. The influences of foundation and substructure stiffness played an insignificant role in this case.

4.2. Stress in the monolithic pier head

The pier strain was recorded on four separately installed rebars (⌀25 mm and 1.7 m long) using pre-applied strain gauges with a recording rate of 500 Hz in the pier axes 42, 43 and 44, cf. Fig. 3. The diameter and the length of the rebars are based on the diameter of the installed reinforcements and their existing anchorage length. Using the distance d between the sensors, the curvature κ can be calculated as

$$\kappa_x = \frac{\varepsilon_{north} - \varepsilon_{south}}{d}, and \kappa_y = \frac{\varepsilon_{west} - \varepsilon_{east}}{d} \quad (1)$$

The curvature κ_x is determined by the respective average value of the corresponding sensor pairing at the north and south sides, whereas the curvature κ_y is given by the single sensor at the west and east sides for the north and south sides respectively e.g., for the curvature evaluation at axis 42, $\kappa_x = \frac{(PS1+PS4)/2-(PS2+PS3)/2}{d1}$, $\kappa_{y\_north} = \frac{PS4-PS1}{d2}$ and $\kappa_{y\_south} = \frac{PS3-PS2}{d3}$.

The definition of positive curvature is based on the right-handed coordinate system, cf. Fig. 11. The curvature around the x-axis is defined as "clockwise" positive in the direction of the x-axis view, while the positive curvature around the y-axis is defined as "counterclockwise" in the direction of the y-axis view.

4.2.1. The influence lines of pier strain and curvature in axes 42 and 44

The measured influence lines of the pier head strains and curvatures represent quantitatively and qualitatively coherent as well as qualitatively comparable deformation behaviour in axes 42 and 44. Nevertheless, the actions resulted in larger curvatures in the pier heads in axis 44, which is attributed to the increased bending stiffness due to the lower pier height. Thus, the pier deformation under quasi-static traffic loads will be demonstrated by the curvatures in axis 44. The curves for each load case (QS1, QS2, and QS3) represent the average results from two round trips, as shown in Fig. 12.

The curves of the curvature around the x-axis show an axisymmetric behaviour. The train passages on the south track (QS1) had positive curvatures around the x-axis, whereas those on the north track (QS2) had negative ones. On the other hand, with double-track actions (i.e., QS3), the curvatures are nevertheless smaller by a power of ten than in the case of single-track action.

The curves of the curvature around the y-axis show a point-symmetric behaviour. The point of symmetry is reached when the centre of the train is in the axis of the considered pier axis (see Fig. 12-bottom). Differences can be seen between the curves of the north and south sides, indicating that there is a non-constant strain distribution across the width of the pier and, consequently, a warping of the pier head. This can be observed in particular with single-track action. The double-track action leads to a uniform strain distribution. Compared to the single-track action, the maximum value increases to only 1.4 times the amount. Fig. 13 shows the load positions of the train at which the maximum and minimum curvature values at axis 42 occur.

4.2.2. The influence lines of pier strain and curvature in axis 43

The pier axis 43 comprises two partial piers as a separating pier. The west pier is monolithically connected to the superstructure of standard block 4 and the east pier to the superstructure of end block Leipzig (cf. Fig. 3). The influence lines of the strains and curvatures at the pier head reflect a qualitative as well as quantitative coherent deformation behaviour for both partial piers. Due to the coupling of the structural blocks by the rail and the H-formed connection of the two piers, a direct and an indirect influence of the action could be observed in the curvature curves in Fig. 14.

It could be seen from the curvature influence line at axis 43-west that when the traffic action loads on the neighbouring east block (i.e. end block on the Leipzig side or abscissa from 0 to 174 m), the unloaded separating pier on the west side already starts to bend slightly in the direction opposite to the direct loading on the considered block, indicating an indirect influence. The effect of CWR plays a major role in the interaction of the two connected structural blocks. A relative displacement between the superstructure and CWR is generated when the bridge moves longitudinally due to the end rotation of the superstructure, leading to a force in the rail caused by friction within rail fasteners. The CWR lays approx. 3 m above the neutral axis of the superstructure and acts like an external tendon. When rotating, this excentric force in the rail results in an interaction of both neighbouring superstructures. The H-formed connection also allows minor transfer of the force between the two neighbouring sections. Both of them could explain why the unloaded superstructure experiences displacements even if the train is on the neighboured section.

The curvatures around the x-axis showed a larger maximum curvature in axis 43 than the ones in axes 42 and 44 under single-track loading (QS1 and QS2). This may be due to the lower bending stiffness of the separating piers that each partial pier has a much smaller thickness than other normal piers. The train passages on the south track (QS1) caused a positive curvature under the direct influence, and the passages on the north track (QS2) led to a negative curvature under the direct influence. With parallel travelling (i.e., double-track action QS3), the load in the pier head is smaller by a power of ten than with single-track action, see Fig. 14-top.

The curvatures around the y-axis are similar to the behaviour of the tilt sensors, especially for parallel runs. This behaviour can also be seen qualitatively in the curvature curves on the loaded pier side for the single-track actions, see Fig. 14-bottom. Similar to axes 42 and 44, a non-constant strain distribution across the pier width and a warping of the pier head also occurred in axis 43 under single-track action. Nevertheless, the warping effect at the separating pier is significantly greater than normal piers since the curvatures around the y-axis in this axis have a larger difference on the north and south sides under single-track loading. Because the superstructure is separated here, allowing larger deformation freedom. Fig. 15 shows the load positions of the train at which the maximum and minimum curvature values occur, using axis 43-west as an example (axis 43-east analogous).

4.2.3. Comparison of the measurement results with the calculated results

As mentioned in the chapter 4.1.2, the FEM with beam elements is not able to simulate the deformation of the cross-section. As a result, only curvatures around the y-axis at the pier head were analysed. The mean values of measured curvatures around the y-axis on the north and south sides were compared with the calculated results in the model. The conversion of the moment into a curvature could be calculated by:

$$\kappa_y = \frac{M_y}{E \bullet I_y} \tag{2}$$

The influence lines of the pier head curvature around the y-axis in axis 42 from measured and calculated results show good qualitative and quantitative agreement in general. Based on the influence lines, the maximum and minimum curvature values in the calculations and measurements in axis 42 could be summarised in Fig. 16.

Compared with the measured values, the best agreement is obtained when the slab track and caps are considered (M2). It could be seen that the absolute extreme curvatures from the measurements are, in general, a little larger (3% on average) than the values from the model with slab track (M2) but much smaller (30% on average) than the values from the model without slab track (M1). On the other hand, the influence of foundation stiffness is very limited since the differences between M1 and M4, as well as between M2 and M3, are very small (max. 1.8%). The curvature at the pier head is, however, significantly influenced by the substructure stiffness, as a 20% reduction of the E-Modulus of piers in M5 resulted in a 17% reduction of the extreme curvature compared to M2.

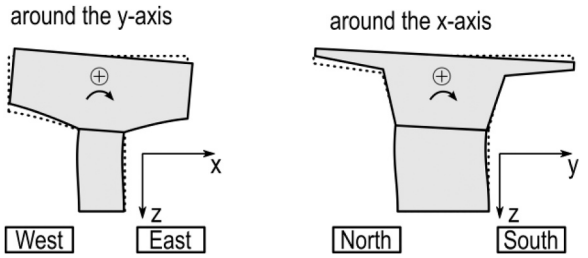

Fig. 11. Definition of positive curvature.

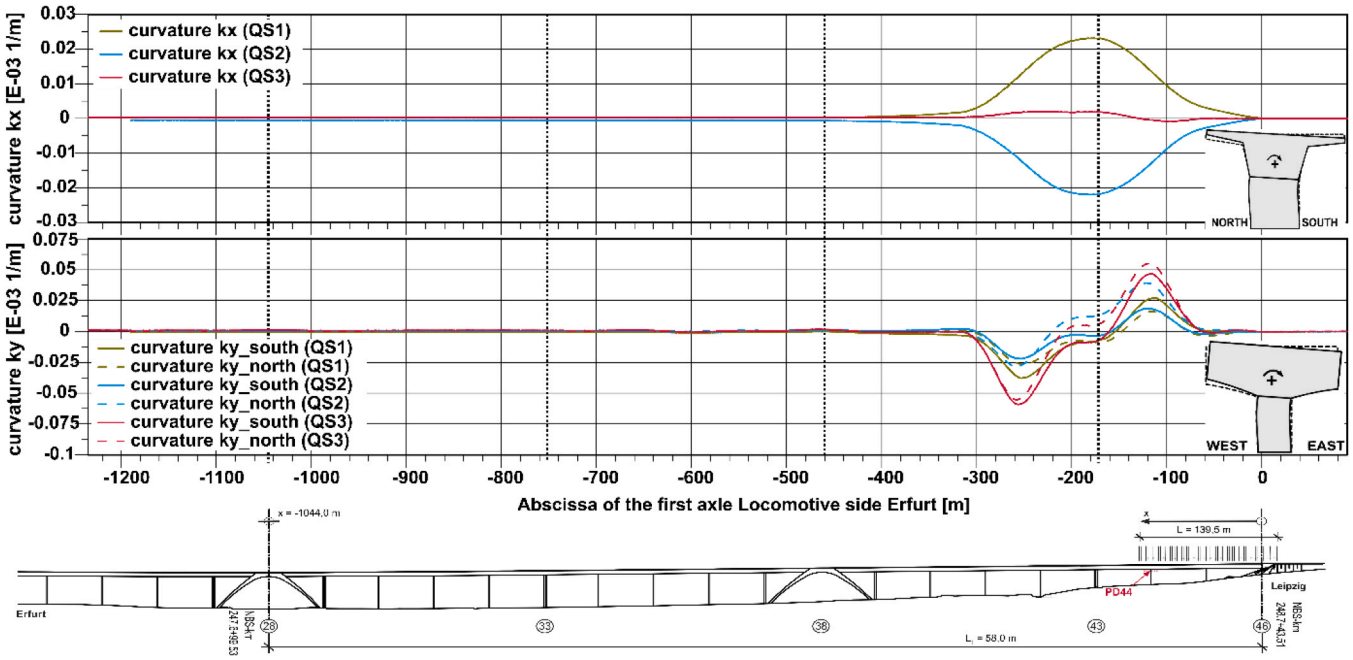

Fig. 12. Influence lines of curvatures in axis 44 under quasi-static loads.

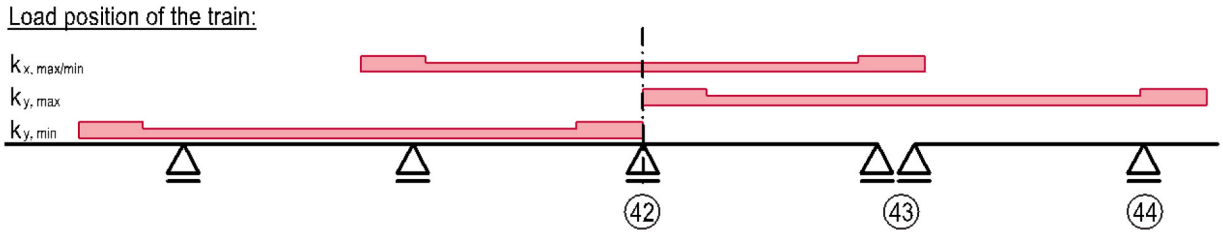

Fig. 13. Decisive load position regarding pier axis 42 (axis 44 analogous).

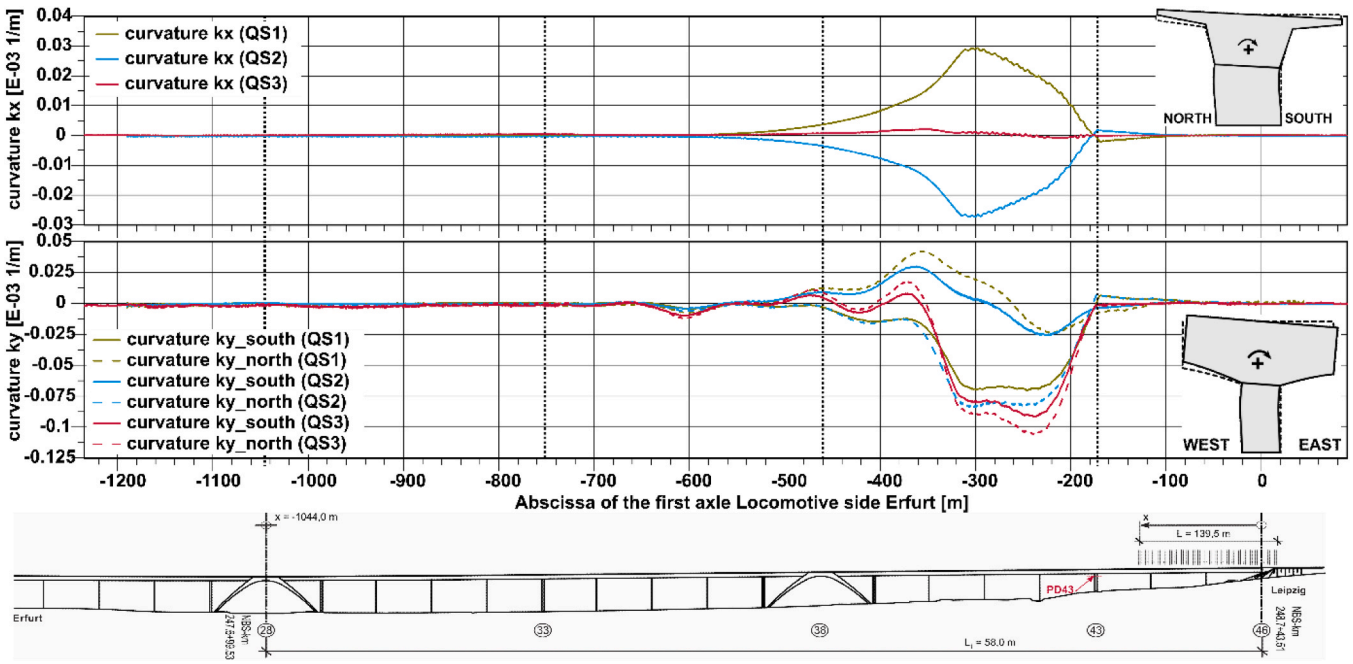

Fig. 14. Influence lines of curvature at axis 43-west under quasi-static loads.

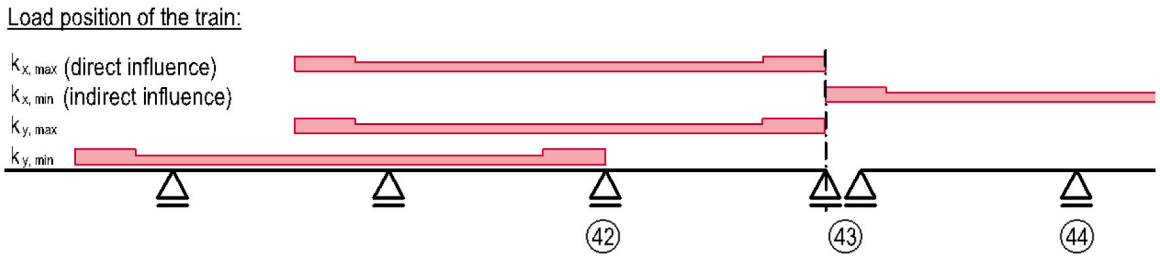

Fig. 15. Decisive load position regarding pier axis 43-west (axis 43-east analogous).

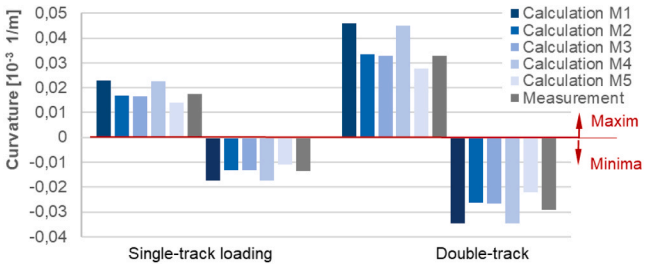

Fig. 16. Extreme calculated and measured curvatures k_y of pier head in axis 42.

4.3. Behaviour under braking loads

4.3.1. Evaluation of the measurement results

The braking force could be calculated as:

$$F_B = M_L \bullet a_{Ef} + \sum_{1}^{i=10} M_{W,i} \bullet a_W + M_L \bullet a_{Le} \tag{3}$$

where M_L and $M_{W,i}$ refer to the weight of the locomotive and single wagon respectively; a_{Ef}, a_{Le} and a_W denote the measured accelerations at the locomotive of the Erfurt side, the locomotive of the Leipzig side, and the Wagon 5 in the middle of the train (cf. Fig. 4). When the maximum braking acceleration is reached, the train is always on the examined section of the structure (cf. Fig. 6). Therefore, the total length of the train is always used for the calculation of the braking force. The positive acceleration measured by the four accelerometers at different train locations is defined in the direction of ascending distance kilometres (i.e., from Erfurt to Leipzig). Thus, the positive horizontal force due to the occurring acceleration is also in the direction of the ascending distance kilometre.

Fig. 17 illustrates the typical evaluation procedure for a braking experiment at BP2 (other braking positions analogous), where the braking force is derived by Eq. (3) and relative longitudinal displacement is the average results of three LVDTs (i.e., JLD.01, JLD.02 and JLD.03) at respective joints. With the initiation of the braking process, a linear increase of the braking force and the longitudinal deformations in the structure joints in axes 33 and 43 can be observed. Shortly before the train reaches a standstill, the values continue to increase by a non-linear component before the maximal braking force is reached and the structure oscillates (cf. Fig. 17). The duration of the braking process, between the initiation of braking and the standstill of the train, is about 5 to 6 s. A frequency of 1.32 Hz can be determined for the oscillation after the braking jerk. It should be noted that the additional mass of the train must be considered here in the vibration system when evaluating the frequency.

From the measured values of the braking force and the relative longitudinal displacement at the construction joints, the stiffness of the structure against longitudinal displacement can be derived. The stiffness was determined from the force-displacement relationship using a linear regression. The linear regression is performed for the time section of the braking process (cf. Fig. 17), which provides a better approximation to the point cloud. The evaluation of the strains and curvatures in the pier axes 43-east and 44 showed no visible stress in the end block Leipzig at braking. Therefore, the relative longitudinal displacement at the joint is assumed to be the absolute displacement of the investigated structural section.

The following Table 2 summarizes the average measured acceleration, the applied braking force, the measured longitudinal displacement, and the resulting structural longitudinal stiffness of train passages at each braking position.

Depending on the braking positions (BP) on the structure and the travelling direction of the train, significant differences can be seen between the determined stiffnesses at the structure joints in axes 33 and 43. The smallest differences in stiffness occur between the axles for BP1 and BP2. The braking forces in these cases are in the direction of the "brake-block" (i.e., the arch pier) and therefore act as compression in the superstructure. For BP3 and BP4, significantly larger differences can be seen between the joints in axes 33 and 43, where braking occurred just

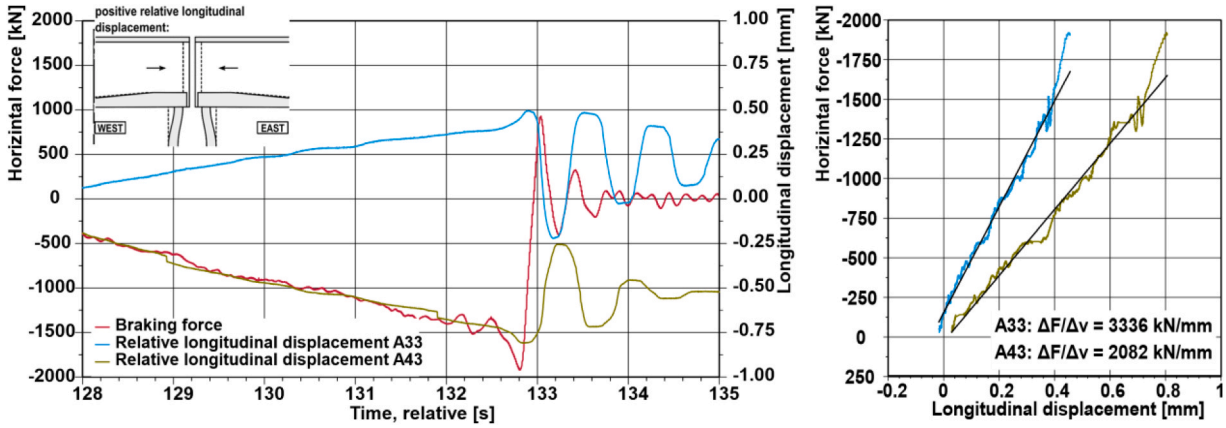

Fig. 17. The evaluation of braking tests.

Table 2
Summary of the average measured results of braking experiments.

		BP1	BP2	BP3	BP4
Braking acceleration [m/s²]	ax1	−2.01	−2.21	−2.05	2.22
	ax2	−2.00	−2.15	−1.99	2.17
	ax3	−1.54	−1.69	−1.58	1.57
	ax4	−1.93	−1.80	−1.90	1.79
Braking force [kN]		1864	1952	1889	1835
Longitudinal displacement [mm]	Axis 33	0.39	0.65	0.76	0.38
	Axis 43	0.51	0.78	0.27	0.79
Longitudinal stiffness [kN/mm]	Axis 33	4826	3014	2385	4992
	Axis 43	3533	2224	11254	2095

before the joints. The direction of the braking force in these targets is away from the "brake-block", and therefore, the braking force acts as a tension in the superstructure. Furthermore, horizontal displacements occur as a result of vertical and horizontal loading (especially for BP1, 3 and 4 near the joint). BP2 is thus most suitable for determining the stiffness under horizontal displacement, where the horizontal force acts centrally on the integrated section and can be concentrated into the "brake-block". The influence of the vertical load on the measured longitudinal displacement is, therefore, small in this case. As a result, the horizontal stiffness of the structure could be determined as 2600 kN/mm from BP2.

4.3.2. Comparison of the measurement results with the calculated results

The calculated results are compared with the measured results from BP2 in Fig. 18. Significant deviations can be seen from the numerical results for static calculation in comparison with the measurement results. These deviations can partly be attributed to the type of action in which the braking force is simulated as a static longitudinal uniform distributed load in the model as assumed in EN 1991–2:2010–12 [30], whereas the braking force actually has a dynamic effect in reality. Dynamic excitation of the bridge structure activates inertia forces that are difficult to quantify. On the other hand, the coupling effect of the continuous welded rail (CWR) with the superstructure at bridge joints is also neglected in the model, which could also lead to different results between measurement and calculation [34]. Especially the longitudinal deformations were assumed as measured relative displacements, the results have some uncertainty due to the relatively small measured displacements. Moreover, the horizontal foundation stiffness could also increase under high load rates for fine-grained soils (i.e., the viscous effect [35]), leading to a stiffer longitudinal behaviour. In this paper, we focus on the comparison between the results of the model for static calculations in the design phase according to Eurocodes and the actual monitoring results. Detailed work on modelling the brake behaviour considering the dynamic effect, track-bridge interaction, and soil viscosity could be carried out in a subsequent study. In general, the determined large longitudinal stiffness is rather dynamic than static stiffness, which also shows the robustness of the structure that is beneficial for railway bridges.

4.4. Dynamic behaviour under high-speed traffic

The dynamic behaviour of the bridge is measured at four positions along the bridge length between axis 40 and axis 43, where each position has two vertical accelerometers and one horizontal accelerometer (cf. Fig. 2). Fig. 19 (a) demonstrates a typical profile of the raw measured accelerations.

4.4.1. Evaluation of the measurement results

From the measurements, the following properties could be characterized: **(1) train speed**, where the average train speed could be calculated by dividing the distance between two light triggers at axes 40 and 43 with the time difference; **(2) maxima and minima of the accelerations** of each sensor at each train passage as shown in Fig. 19 (a), where raw measurement data without filtering were used; **(3) horizontal and vertical natural frequency**, where the decay process was isolated in the time signal, cf. Fig. 19 (b), so that interference effects from the forced vibrations caused by the train crossing were not taken into account. Since the two light triggers could easily identify the wheel axles of the train, the free vibration parts (i.e., decay process) were chosen after all the wheel axles passed the two light triggers (i.e., the train left the testing area). By applying the Fast Fourier Transform (FFT), the time course signal could be transformed into the frequency domain. The frequency spectrum was analysed using the peak picking method to determine natural frequencies, see Fig. 19 (c); **(4) eigenform**, in which the measured signals were filtered through a bandpass for the respective natural frequency during the decay process. The mode shapes were then identified by comparing the amplitudes and phase shifts of the filtered signals at all measurement positions. For the determination of the vertical eigenmodes, the pier axis was assumed to be zero points of motion; **(5) damping ratio**, where the logarithmic damping decrement Λ was determined from the acceleration maximum $a(t)$ at time t_1 and the n^{th} subsequent acceleration maximum after bandpass of the acceleration curve in decay process for respective natural frequency [36].

$$\Lambda = \frac{1}{n}\ln\frac{a(t_1)}{a(t_2)} \tag{4}$$

The damping ratio D can be further calculated to

$$D = \frac{\Lambda}{\sqrt{(2\pi)^2 + \Lambda^2}} \tag{5}$$

To assess the dynamic stability of the structure, the development of the occurred accelerations is investigated over the entire velocity spectrum. The maxima and minima of vertical and horizontal accelerations in relationship to the train velocity for all 68 train passages crossing both the south and north tracks at four measuring positions along bridge length are described in Fig. 20.

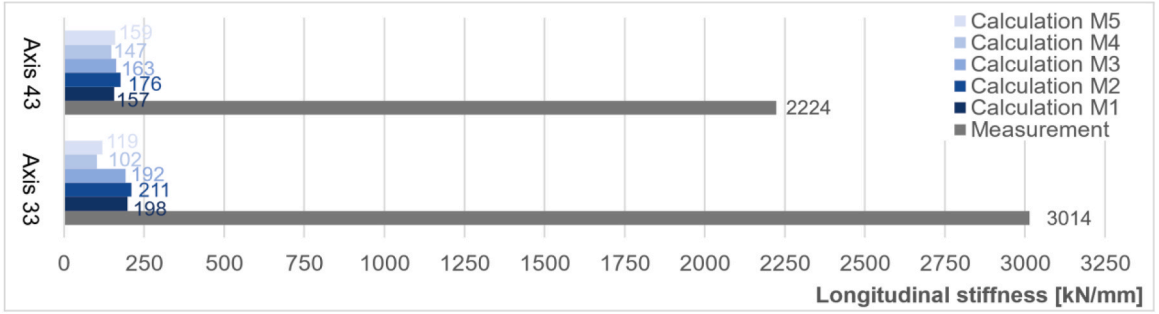

Fig. 18. Calculated and measured longitudinal stiffness at BP2.

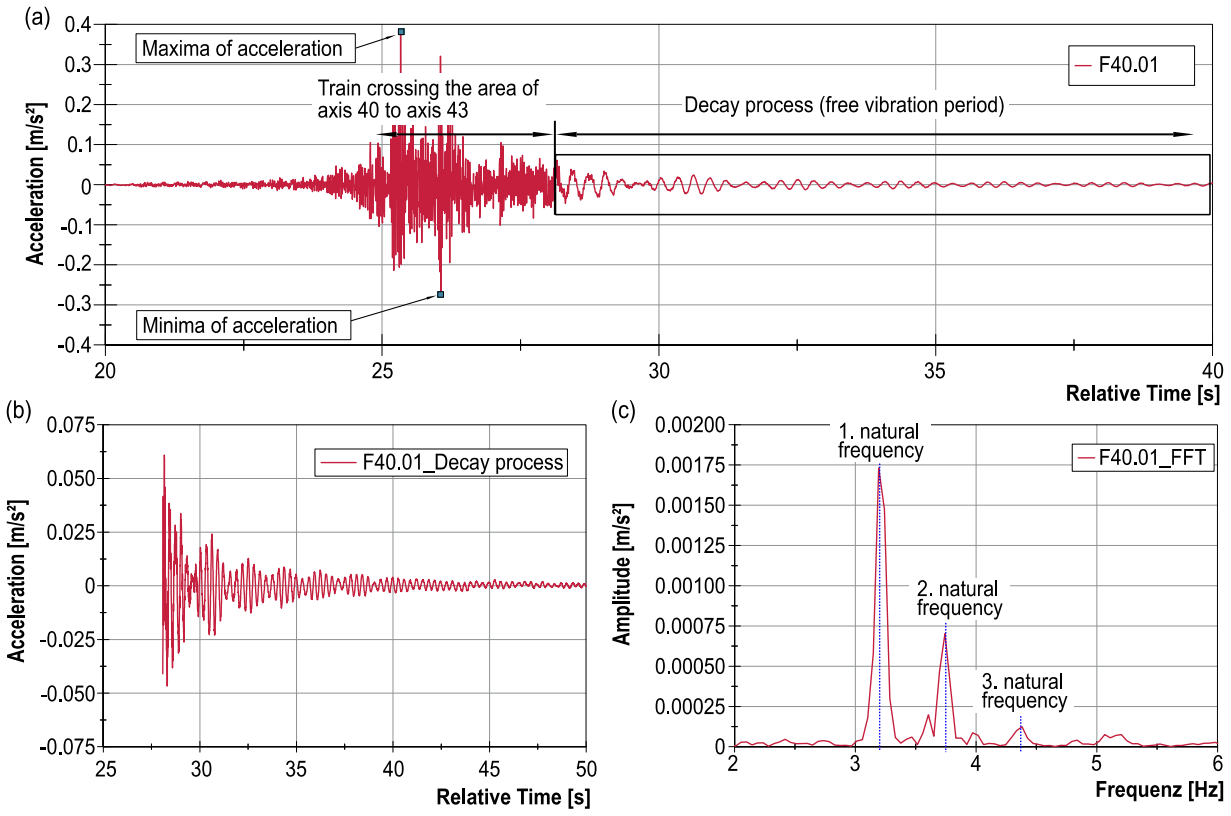

Fig. 19. Dynamic analysis: (a) typical profile of the acceleration; (b) decay process of acceleration for the free vibration period; (c) Fast Fourier Transform (FFT) analysis.

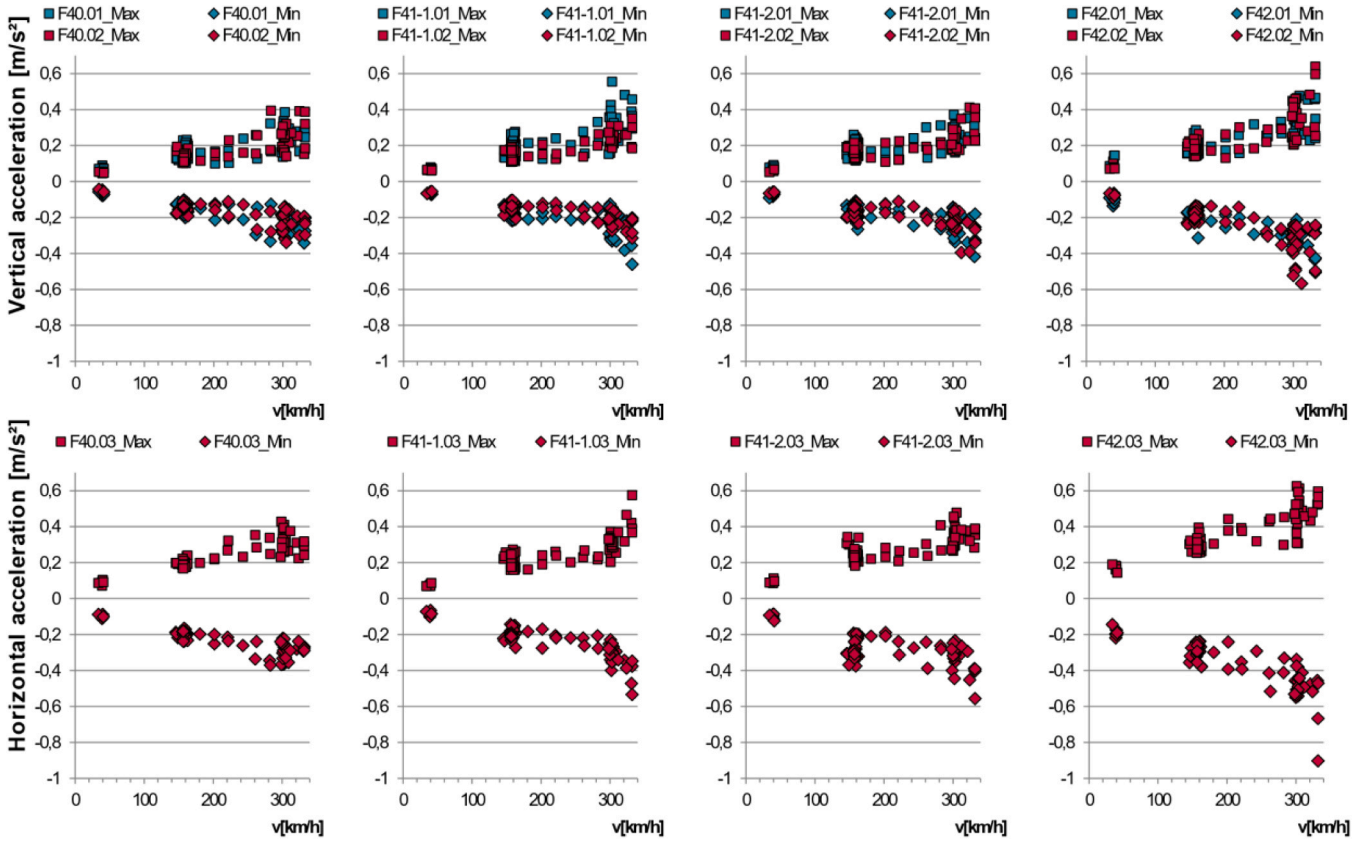

Fig. 20. Maxima and minima of the vertical and horizontal accelerations as a function of ICE-S train speed for all the train passages on both south and north tracks.

It could be found that both vertical and horizontal accelerations become greater with increasing speed. At high speeds (v > 300 km/h), a disproportionate correlation can be observed. The measured maximum accelerations in the range of −0.9 m/s² to 0.65 m/s² remain nevertheless very low compared to the permissible values for slab track. Furthermore, the influence of travel directions was also investigated. For all the train passages on the south track, the two travelling directions have no influence on the measured accelerations.

Finally, The average values of the natural frequency, damping ratio, and corresponding eigenform measured from 3 train passages on the south track with a speed of about 300 km/h on the same day are summarised in Table 3 based on the abovementioned methods. For each train passage, the horizontal properties were obtained from the average values of the horizontal accelerometers (A.03) at 4 measurement positions; meanwhile, the vertical properties were gained from the average values of the 8 vertical accelerometers (A.01 and A.02). It's also noted during the evaluation, that the measured scatter in natural frequencies derived from each sensor is very small, but the variation in the damping ratio is much larger. It is probably because artificially selecting different subsequent n^{th} acceleration after maximum when calculating the damping ratio is more stochastic than using the FFT algorithm when determining the natural frequencies.

4.4.2. *Comparison of the measurement results with the calculated results*

To investigate the influence of the slab track, parametric evaluation is as follows:

- M_noSlab: dealing with neither mass nor stiffness of the slab track;
- M_noStiff: considering only the mass and eliminating the stiffness of the slab track;
- M_withSlab: taking into account both the mass and stiffness of the slab track.

Fig. 21 summarized the natural frequencies of various eigenmodes in measurements and calculations. The calculation results show that significant changes in the natural frequencies occur due to the consideration of the slab track. The increase in stiffness has a smaller effect on the magnitude of the natural frequency than the increase in mass. This is because the box girder basically already has a relatively large stiffness. In the structural analysis, it is common to consider the masses as additional loads, but to neglect the contribution to the stiffness, i.e. M_noStiff, in which the calculated natural frequencies are usually smaller than measured ones. This result can be considered positive with respect to the vertical behaviour of the structure. In this study, the best agreement with the measurement results is nevertheless achieved when the slab track is completely neglected. Since the measured results were limited in SB4 and the track-bridge interaction was also neglected in the model, more research is needed to verify this conclusion. The influence of slab track on horizontal behaviour is, in general, smaller than on vertical behaviour.

5. Conclusion and outlook

This paper presents a comprehensive investigation into the structural behaviour of the Unstrut Viaduct, a long semi-integral HSRB, under different traffic loads using both SHM and numerical simulation. The actual behaviour of the bridge aligned with the design predictions, satisfying the requirements for flexibility under quasi-static loads and rigidity under braking and high-speed loads. The key scientific findings are as follows:

(1) The pier curvature around the y-axis is more decisive than around the x-axis. Moreover, The separating pier exhibited a significantly larger warping effect under single-track loading than normal piers due to the separated superstructure and reduced pier stiffness. A complex interaction of the two structural blocks at the separated pier due to the coupling of the CWR and the H-formed connection of the two partial piers was also observed in the curvature curves by the indirect influence on the neighbouring block.
(2) The determined dynamic longitudinal stiffness of the bridge under braking loads was 12 times higher than that predicted by static calculations due to the inertia forces in dynamic scenarios, increased foundation stiffness under high load rates, and the track-bridge interaction, which demonstrates nevertheless the robustness and great load-bearing potential of the semi-integral HSRB.

Table 3
Dynamic properties of Unstrut Viaduct for the area between axes 40 and 43.

Description	Eigenform		Natural frequency [Hz]	Damping ratio
	Measured	FEM		
1. horizontal Eigenform	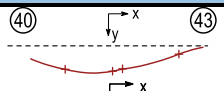		0.69	2.11%
2. horizontal Eigenform	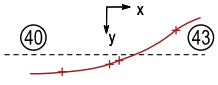	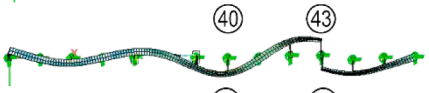	1.00	4.09%
3. horizontal Eigenform	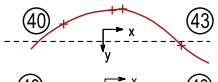		1.28	3.71%
1. vertical Eigenform	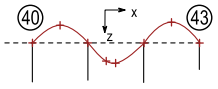	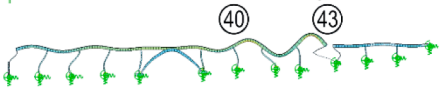	3.21	0.87%
2. vertical Eigenform	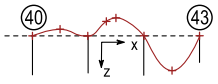		3.73	0.94%
3. vertical Eigenform	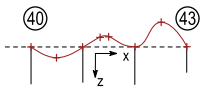	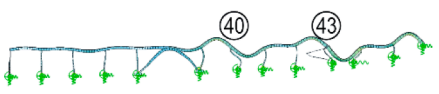	4.35	0.90%

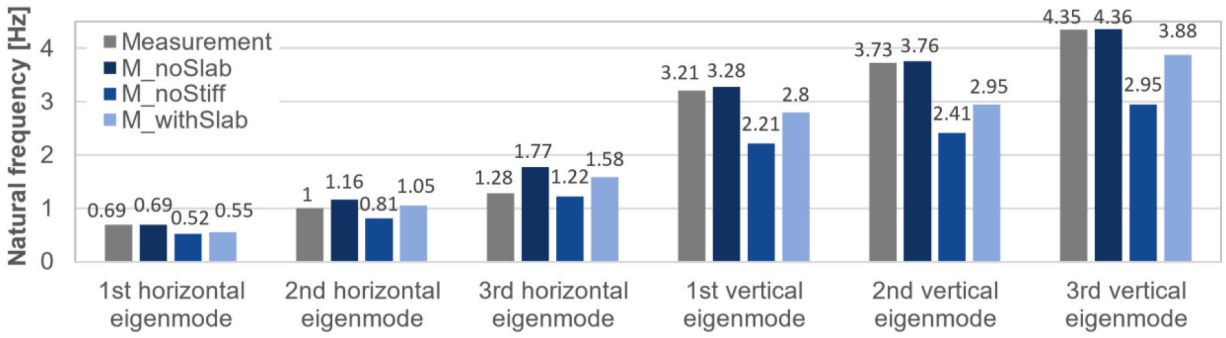

Fig. 21. Comparison of natural frequency between measurements and calculations.

(3) The structure experienced a disproportionate increase in vertical and horizontal accelerations under high-speed loads exceeding 300 km/h. However, the observed accelerations (−0.9 m/s^2 - 0.65 m/s^2) remained within permissible limits, confirming the viability of the semi-integral design for high-speed rail applications.
(4) The initial assumption in the static calculation to consider the slab track as external loads without stiffness is a conservative approach. Nevertheless, including both the mass and stiffness of the slab track in the model provides more realistic predictions. Future models should account for dynamic effects, track-bridge interaction, and variations in the foundation stiffness under high load rates.

These findings provide valuable insights into the behaviour of semi-integral HSRB and offer guidance for improving the accuracy of structural models. Through accurate prognosis of the structure, the digital twin of important infrastructures could be built for the construction, operation, and maintenance phases to guarantee a safer and longer utilization of the reinforced concrete structure, contributing to the important topic of CO_2 reduction nowadays.

Author Agreement Statement

We the undersigned declare that this manuscript is original, has not been published before and is not currently being considered for publication elsewhere.

We confirm that the manuscript has been read and approved by all named authors and that there are no other persons who satisfied the criteria for authorship but are not listed. We further confirm that the order of authors listed in the manuscript has been approved by all of us.

We understand that the Corresponding Author is the sole contact for the Editorial process. He/she is responsible for communicating with the other authors about progress, submissions of revisions and final approval of proofs.

CRediT authorship contribution statement

Martin Classen: Writing – review & editing. **Steffen Marx:** Supervision, Resources, Project administration, Funding acquisition. **Max Käding:** Visualization, Methodology, Investigation, Formal analysis, Data curation. **Marc Wenner:** Writing – review & editing, Visualization, Methodology, Investigation, Formal analysis, Data curation, Conceptualization. **Sisi Zhang:** Writing – review & editing, Writing – original draft, Visualization, Validation, Methodology, Investigation, Formal analysis, Data curation, Conceptualization.

Declaration of Competing Interest

The authors declare that they have no known competing financial interests or personal relationships that could have appeared to influence the work reported in this paper.

Data availability

The authors do not have permission to share data.

References

[1] Marx S, Seidl G. Integral railway bridges in Germany. Struct Eng Int 2011;21(3):332–40.
[2] Su M, Dai G, Marx S, Liu W, Zhang S. A brief review of developments and challenges for high-speed rail bridges in China and Germany. Struct Eng Int 2019;29(1):160–6.
[3] Schenkel M, Marx S, Krontal L. Innovative Großbrücken im Eisenbahn-Hochgeschwindigkeitsverkehr am Beispiel der Neubaustrecke Erfurt-Leipzig/Halle. Beton- und Stahlbetonbau 2009;104(11):782–9.
[4] Marx S, Krontal L, Bätz S, Vehlow A. Die Scherkondetalbrücke, die erste semi-integrale Talbrücke der DB AG auf der Neubaustrecke Erfurt – Leipzig/Halle VDE 8.2. Beton- und Stahlbetonbau 2010;105(3):134–41.
[5] Schlaich Jörg, Fackler Thomas, Weißbach Matthias, Schmitt Victor, Ommert Christian, Marx Steffen, Krontal Ludolf. Leitfaden Gestalten von Eisenbahnbrücken DB Netz. Hamburg: Eurailpress DVV Media Group; 2009.
[6] Herbers M, Wenner M, Marx S. A 576 m long creep and shrinkage specimen – Long-term deformation of a semi-integral concrete bridge with a massive solid cross-section. Struct Concr 2023;24(3):3558–72.
[7] Marx S, Wenner M. Structural Health Monitoring (SHM) an der Scherkondetalbrücke: Eine semi-integrale Eisenbahn-Betonbrücke. Beton- und Stahlbetonbau 2015;110(S2):2–8.
[8] Wenner M, Meier T, Wedel F, Schacht G, Marx S. Experimental Determination of the Longitudinal Pier Stiffness of a Long Railway Viaduct. Front Built Environ 2019;5.
[9] Mehlhorn G, Curbach M. Handbuch Brücken: Entwerfen, Konstruieren, Berechnen, Bauen und Erhalten. 2nd ed. Berlin, Heidelberg: Springer Berlin Heidelberg; 2010.
[10] Kaufmann W, Alvarez M. Swiss federal roads office guidelines for integral bridges. Struct Eng Int 2011;21(2):189–94.
[11] Berger D, Graubner C-A, Pelke E, Zink M. Besonderheiten bei Entwurf und Bemessung integraler Betonbrücken. Beton- und Stahlbetonbau 2004;99(4):295–303.
[12] Engelsmann S. Entwerfen und Bemessen von Betonbrücken ohne Fugen und Lager. Zugl.: Stuttgart. Univ., Diss., 1998 u.d.T.: Engelsmann, Stephan: Integrale Betonbrücken Entwerfen und Bemessen von Brücken ohne Lager und Fugen. 01th ed.,. Berlin: Beuth,; 1999.
[13] Glitsch W. Richtlinie "Integrale Bauwerke" – Sachstandsbericht. Stahlbau 2013;82(10):708–14.
[14] Schüller M. Konzeptionelles Entwerfen und Konstruieren von Integralen Betonbrücken. Beton- und Stahlbetonbau 2004;99(10):774–89.
[15] Russo G, Bergamo O, Damiani L. Retrofitting a short span bridge with a semi-integral abutment bridge: the treviso bridge. Struct Eng Int 2009;19(2):137–41.
[16] Shid Moosavi SS, rahaie ar. The performance of integral and semi-integral pre-tensioned concrete bridges under seismic loads in comparison with conventional bridges. AUT J Civ Eng 2018.
[17] Schneider S, Marx S. Design of railway bridges for dynamic loads due to high-speed traffic. Eng Struct 2018;174:396–406.
[18] Bakeer R.M., Mattei N.J., Almalik B.K., Carr S.P., Homes D. Evaluation of DOTD semi-integral bridge and abutment system; 2005.
[19] Dietz J. Besonderheiten bei der Ausführung semi-integraler Großbrücken am Beispiel der Wehretalbrücke. Beton- und Stahlbetonbau 2019;114(6):430–9.
[20] Jin X, Shao X, Peng W, Yan B. A new category of semi-integral abutment in China. Struct Eng Int 2005;15(3):186–8.
[21] Silva PH, Costa YD, Walter JR, Kouchaki BM, Zornberg JG, Costa CM. Numerical evaluation of a semi-integral bridge abutment under cyclic thermal movements. Transp Geotech 2023;39:100938.
[22] Schiefer S, Fuchs M, Brandt B, Maggauer G, Egerer A. Besonderheiten beim Entwurf semi-integraler Spannbetonbrücken: Eine Alternative im Brückenbau mit

zunehmender Bedeutung – aufgezeigt am Beispiel der Fahrbachtalbrücke im Zuge der BAB A3 bei Aschaffenburg. Beton- und Stahlbetonbau 2006;101(10):790–802.
[23] Jung B, Morgenthal G, Xu D. Integrative sensitivity analysis applied to semi-integral concrete bridges. J Bridge Eng 2014;19(6).
[24] Gebauer D, Stümpel M, Haar C, von der, Marx S. Criteria and influencing parameters for the design of piers of semi-integral bridges. Struct Concr 2018;19(2):625–34.
[25] Gregor Schacht Frederik Wedel, Marx Steffen, editors. Bridge Load Testing in Germany. Anaheim, USA: Evaluation of Concrete Bridge Behavior Through Load Testing - International Perspectives at the ACI Fall 2017 Convention; 2017.
[26] Structural health monitoring of the Scherkondetalbrücke: A semi integral concrete railway bridge. Leipzig, Germany: 4th International Conference on. In: Marx S, Wenner M, editors. Concrete Repair, Rehabilitation and Retrofitting, 2015. ICCRRR; 2015.
[27] Wenner M, Käding M, Marx S. Messtechnische Überwachung bei Brückenbaumaßnahmen. Bautechnik 2018;95(1):44–52.
[28] Käding M, Wenner M, Liao H, Marx S, editors. Determination and assessment of the behavior of a semi-integral railway viaduct. Ghent, Belgium: the 6th International Symposium on Life-Cycle Civil Engineering (IALCCE 2018): Towards an Integrated Vision; 2018.
[29] DIN EN 1992-2:2010-12. German Version of Eurocode 2 - Design of concrete structures - Part 2: Concrete bridges - Design and detailing rules. Berlin, Germany: Beuth Verlag Gmb; 2010.
[30] DIN EN 1991-2:2010-12. German version of Eurocode 1: Actions on structures - Part 2: Traffic loads on bridges. Berlin, Germany: Beuth Verlag Gmb; 2010.
[31] DIN Fachbericht 101:2009-03. Actions on Bridge. Berlin, Germany: Beuth Verlag Gmb; 2009.
[32] Deutsche Gesellschaft für Geotechnik e.V. (ed.). Empfehlungen des Arbeitskreises "Pfähle". EA-Pfähle. 2nd ed. Berlin: Ernst; 2013.
[33] DB Netz A.G. Ril 804.4501- German guideline for integral and semi-integral railway bridges. Frankfurt am Main; 2021.
[34] Wenner M, Lippert P, Plica S, Marx S. Längskraftabtragung auf Eisenbahnbrücken: Teil 1: Geschichtliche Entwicklung und Modellbildung. Bautechnik 2016;93(2):59–67.
[35] Niemunis A. Extended hypoplastic models for soils. Bochum: Ruhr-Univ; 2003.
[36] Zhang S., Marx S., Wenner M. (eds.). Behavior of transition plates crossing high-speed railway bridge joints in Germany. Vancouver, Canada: 39th IABSE Symposium; 2017.